Petereit, J., Saynisch, J., Irrgang, C., Thomas, M. (2019): Analysis of ocean tide induced magnetic fields derived from oceanic in-situ observations — climate trends and the remarkable sensitivity of shelf regions. - *Journal of Geophysical Research*, *124*, 11, pp. 8257—8270.

DOI: http://doi.org/10.1029/2018JC014768

JGR Oceans

RESEARCH ARTICLE
10.1029/2018JC014768

Analysis of Ocean Tide-Induced Magnetic Fields Derived From Oceanic In Situ Observations: Climate Trends and the Remarkable Sensitivity of Shelf Regions

Johannes Petereit[1,2], Jan Saynisch-Wagner[1], Christopher Irrgang[1], and Maik Thomas[1,2]

[1]GFZ German Research Centre for Geosciences, Potsdam, Germany, [2]Institute of Meteorology, Freie Universität Berlin, Berlin, Germany

Key Points:
- Magnetic signals estimated from in situ temperature and salinity observations correlate well with oceanic heat content variations
- The derived magnetic field amplitude and ocean heat content trends match the expectations of previous studies
- Variations in oceanic tidal magnetic fields are largest in shelf regions, which allow a targeted monitoring of oceanic climate there

Supporting Information:
- Supporting Information S1
- Supporting Information S2
- Supporting Information S3
- Supporting Information S4
- Supporting Information S5
- Supporting Information S6

Correspondence to:
J. Petereit
petereit@gfz-potsdam.de

Citation:
Petereit, J., Saynisch-Wagner, J., Irrgang, C., & Thomas, M. (2019). Analysis of ocean tide-induced magnetic fields derived from oceanic in situ observations: Climate trends and the remarkable sensitivity of shelf regions. *Journal of Geophysical Research: Oceans*, *124*, 8257–8270. https://doi.org/10.1029/2018JC014768

Received 14 NOV 2018
Accepted 2 OCT 2019
Accepted article online 8 NOV 2019
Published online 25 NOV 2019

Abstract Tidal motion of oceanic salt water through the ambient geomagnetic field induces periodic electromagnetic field signals. Amplitudes of the induced signals are sensitive to variations in electrical seawater conductivity and, consequently, to changes in oceanic temperature and salinity. In this paper, we computed and analyzed time series of global ocean tide-induced magnetic field amplitudes. For this purpose, we combined data of global in situ observations of oceanic temperature and salinity fields from 1990–2016 with data of oceanic tidal flow, the geomagnetic field, mantle conductivity, and sediment conductance to derive ocean tide-induced magnetic field amplitudes. The results were used to compare present day developments in the oceanic climate with two existing climate model scenarios, namely, global oceanic warming and Greenland glacial melting. Model fits of linear and quadratic long-term trends of the derived magnetic field amplitudes show indications for both scenarios. Also, we find that magnetic field amplitude anomalies caused by oceanic seasonal variability and oceanic climate variations are 10 times larger in shallow ocean regions than in the open ocean. Consequently, changes in the oceanic and therefore the Earth's climate system will be observed first in shelf regions. In other words, climate variations of ocean tide-induced magnetic field amplitudes are best observed in shallow ocean regions using targeted monitoring techniques.

1. Introduction

Throughout Earth's history, the global climate changed drastically from extreme cold to extreme warm phases. Since ocean currents distribute heat from solar radiation throughout the globe, the ocean plays a central role in climate formation. The release of oceanic heat and humidity into the atmosphere is one of the driving forces for atmospheric circulation. Atmosphere and ocean dynamics impact each other mutually and form a complex dynamical system, which determines the global climate.

Global mean surface temperature and ocean heat content (OHC) have risen over the last 50 years (Hansen et al., 2010; Levitus et al., 2012). Changes in ocean circulation, and therefore global heat transport, are the consequence. In order to monitor global climate variations, it is essential to observe oceanic processes continuously (Meyssignac et al., 2019).

In principle, global monitoring of climate variations can be achieved with observations of ocean tide-induced magnetic field signals (Irrgang et al., 2019; Saynisch et al., 2016, 2017). Electric currents are induced by the motion of electrically conducting seawater through the ambient geomagnetic field (Irrgang et al., 2016; Manoj et al., 2006; Minami, 2017). The strength of the induced electric currents and the corresponding magnetic fields is, among other influences, sensitive to changes in the electrical seawater conductivity (σ) distribution, which is determined by oceanic temperature and salinity. That the oceanic σ distribution can be used to anticipate OHC with great precision and accuracy has recently been demonstrated by Trossman and Tyler (2019).

Tidal current-induced magnetic field signals reach values of several nanoteslas (nT) at sea level and satellite altitude (Kuvshinov, 2008; Minami, 2017). Due to the periodicity of the induced magnetic field signals, it has been possible to extract global distributions of radial semidiurnal principal lunar tide (M2)-induced magnetic field ($B_{M2,r}$) amplitudes from satellite observations of the magnetic field missions CHAMP (Sabaka et al., 2015; Tyler et al., 2003) and Swarm (Sabaka et al., 2016, 2018). Additionally, Grayver and

Olsen (2019) have successfully extracted the magnetic field signals of the tidal constituents N2 and O1 from combined data of both satellite missions. By means of an artificial neural network, it is possible to infer global ocean heat content values from these global ocean tide-induced magnetic field amplitudes (Irrgang et al., 2019).

Ocean tide-induced electric currents are sensitive to electrical seawater conductivity, tidal ocean flow, and the geomagnetic field. Out of these three, conductivity exhibits the highest temporal variability. In fact, variations of oceanic temperature and salinity occur on shorter time scales than changes in the tidal ocean flow or the geomagnetic field. This fact was used in recent studies that investigated $B_{M2,r}$ amplitude variations due to climate variations. On one hand, Saynisch et al. (2017) modeled the impact of the oceanic warming, caused by increased greenhouse gas content in the atmosphere, on the ocean tide-induced magnetic fields. It has been found that, in general, $B_{M2,r}$ amplitudes increase with oceanic warming. On the other hand, motivated by Greenland glacial melting, Saynisch et al. (2016) have simulated a continuous freshwater influx in the arctic region, which has led to a breakdown of the Atlantic meridional overturning circulation (AMOC) in the model simulation. In contrast to the first study, altered heat transport and an increase in cold freshwater caused a decrease in $B_{M2,r}$ amplitudes.

Since, in both simulations the individual processes were investigated separately, it is currently unknown, whether one process will dominate or whether the two processes will annihilate each other in time. Moreover, it is unknown how the actual ocean climate influences $B_{M2,r}$ amplitudes and how variations in the amplitudes compare to modeled climate scenarios. Currently, there are no global magnetic field observations with the necessary precision and temporal resolution to answer that question by extracting $B_{M2,r}$ amplitude variations. But, the necessary global $B_{M2,r}$ amplitudes can be modeled, based on recent ocean state observations. In this study, we computed and analyzed a time series of monthly mean global $B_{M2,r}$ amplitudes for the years 1990 to 2016 based on global oceanic temperature and salinity observations. Dynamical changes in the resulting time series were then linked to recent ocean dynamics and compared to the findings of the preceding studies.

In section 2 we present the data and the methods used to compute the $B_{M2,r}$ amplitudes. The results of the subsequent analysis are presented in section 3 and discussed in section 4. We conclude and summarize this study in section 5.

2. Data and Methods

2.1. Oceanographic In Situ Observations

The oceanographic data needed to calculate recent changes in the ocean tide-induced magnetic fields is provided by the Copernicus Marine Environment Monitoring Service. The Coriolis data set for Re-Analysis (CORA5.0; Cabanes et al., 2013), with global monthly mean seawater temperature and salinity fields, is used to compute ocean tide-induced electric currents and monthly mean oceanic conductance models.

In the CORA5.0 data set, in situ measurements of observation techniques such as Argo floats (Roemmich et al., 2009), moored buoys (e.g., TAO/TRITON network Hayes et al., 1991), or gliders are used to estimate monthly mean temperature and salinity fields through a statistical analysis method, the In Situ Analysis System (Bretherton et al., 1976; Gaillard et al., 2016). The first guess for their estimation method was derived from the monthly climatologies of temperature and salinity distribution of the World Ocean Atlas (WOA) (Locarnini et al., 2013; Zweng et al., 2013). The WOA climatologies for periods between 1985–1994, 1995–2004, and 2005–2012 are interpolated to provide monthly temperature and salinity fields centered at the 15th of each month. After applying an objective analysis, the resulting fields contain dynamical changes on interannual, interseasonal, and monthly time scales from 1990 to 2016 on a $0.5° \times 0.5°$ grid. The data are distributed on 152 vertical levels between the sea surface and a depth of 2,000 m.

The in situ observation coverage is low in the first 10 years of the considered period but increases with the progressive deployment of Argo floats. Almost no data are available in the polar regions, which have been shown to be highly susceptible to climate variations (Saynisch et al., 2016, 2017). In the highly dynamic, and for this study crucial, region of the northern Atlantic, by contrast, data coverage is particularly high. In case of unavailable profile data, the provided values are equal to the first guess, which is equal to the temperature and salinity fields of the WOA.

2.2. Conductivity Model

The conductivity model is composed of a time-constant spherically symmetric 1-D mantle conductivity (Grayver et al., 2017) placed below a thin spherical electrical conductance layer. The spherical layer combines the time-constant sediment conductance with the time-variable ocean conductance. The sediment conductance is calculated with the method of Everett et al. (2003) using sediment thicknesses from Laske and Masters (1997).

This study uses monthly mean ocean conductance fields that contain monthly, interseasonal, and interannual variability. There are precomputed global σ distributions available (Tyler et al., 2017). These data sets have been compiled with the highest possible consistency in ocean data in mind assuring that only temperature and salinity were used that were measured at the same place and time. However, these distributions present average climatologies and lack the necessary interannual variability and long-term trends needed to analyze the relation between the underlying changes in ocean dynamics and the ocean tide-induced magnetic field signals. Hence, we computed the monthly mean ocean conductance from the oceanic seawater temperature and salinity distribution of the CORA5.0 data set with the following three-step algorithm:

First, we derived the 3-D oceanic conductivity distribution down to a depth of 2,000 m from the CORA temperature and salinity fields (cf. section 2.1). The conductivity was computed with the Gibbs-Seawater equation, specifically, the conductivity function of the TEOS-10 toolbox (IOC et al., 2010). The ocean pressure p needed for this calculation was approximated as $p \approx h$ in dbar. Here, h is the depth of the individual data point given in m. Subsequently, the monthly conductivity was depth-integrated down to 2,000 m depth to obtain oceanic conductance fields of the upper ocean.

Second, the global ocean conductance from sea surface to ocean bottom was computed by adding the deep ocean conductance for depths below 2,000 m to the upper ocean conductance (cf. step one). The deep ocean conductance was obtained by integrating the global conductivity distribution of the WOA for the years 1981 to 2010, from 2,000 m to ocean bottom (Tyler et al., 2017).

Third, the obtained monthly ocean conductance fields were depth-averaged (σ_{mean}) first and then multiplied with the bathymetry of the TPXO8-atlas (Egbert and Erofeeva, 2002). This way, we removed the influence of the coarse bathymetry resolution of the WOA in the global ocean conductance fields. Furthermore, this step assures consistency between the conductance and the ocean tide-induced electric currents. The latter rely on the tidal flow of the semidiurnal ocean tide M2, which was also taken from the TPXO8-atlas (cf. section 2.3).

The final monthly mean ocean conductance fields have a regular grid with a resolution of 0.5° × 0.5°. All necessary input fields have been interpolated bi-linearly to fit this regular grid before applying the algorithm.

2.3. Electric Current

The Lorentz force acts on seawater that flows through the ambient geomagnetic field. As a consequence, an electric current is induced. We compute the electric current sheet density $\vec{j}_{M2}$ induced by the tidal ocean currents of the semidiurnal principal lunar tide M2 with Ohm's Law:

$$\vec{j}_{M2}(\varphi,\vartheta) = \sigma_{mean}(\varphi,\vartheta)\left(\vec{V}_{M2}(\varphi,\vartheta)\times\vec{B}_{Earth}(\varphi,\vartheta)\right). \quad (1)$$

Here, φ and ϑ are longitude and colatitude; σ_{mean}, $\vec{V}_{M2}$ and $\vec{B}_{Earth}$ are the depth-averaged conductivity (cf. section 2.2), the tidal ocean transport of the M2 tide, and the geomagnetic field, respectively.

For the tidal flow of the M2 tide $\vec{V}_{M2}$, we use the barotropic flow provided by the TPXO8-atlas (Egbert and Erofeeva, 2002). The geomagnetic field $\vec{B}_{Earth}$ is based on the international geomagnetic reference field IGRF-12 (Thébault et al., 2015). We follow the approach of the Greenland glacial melting study (Saynisch et al., 2016) and the oceanic warming study (Saynisch et al., 2017) and assume a time-constant $\vec{B}_{Earth}$. This assures better comparability between the findings of all three studies and puts the focus on the oceanic causes of $B_{M2,r}$ variability. However, the influence of the secular variation on $\vec{j}_{M2}$ should be considered when the data set of this study is compared to actual $B_{M2,r}$ observations. Since the variations in the geomagnetic field are well known (Gillet et al., 2010), their effects can be removed.

2.4. Induction Solver x3dg

The time-varying electric currents induced by the oceanic tidal motion produce time-varying magnetic fields. These magnetic fields in return interact with their electrical conducting environment and induce

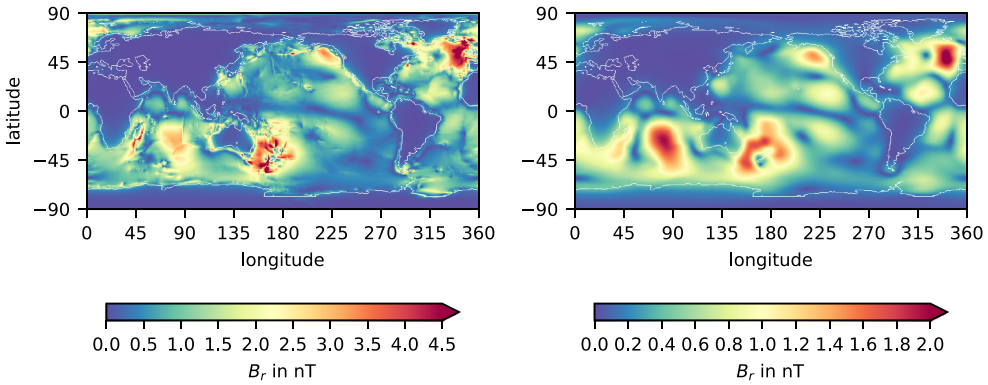

Figure 1. Amplitudes of the radial magnetic field component induced by the oceanic M2 tide. Temporal average over the whole time span from 1990 to 2016. The amplitudes at sea level (left) reach higher magnitudes and are more detailed in their lateral structure. At satellite altitude (right), the amplitudes have decreased in magnitude. Also, the influence of small-scale structures with high amplitudes at sea level vanishes due to the upward continuation of the signals.

secondary electric currents, which produce further magnetic fields and so forth. This mechanism and additional electromagnetic phenomena such as galvanic effects and currents induced parallel to conductivity boundaries are described by Maxwell's equations.

Maxwell's equations have no analytical solution in a general three-dimensional environment. With the numerical 3-D induction solver x3dg of Kuvshinov (2008), we compute the electromagnetic response to interactions of ocean tide-induced currents and the heterogeneous electrical conducting environment; x3dg solves Maxwell's equations in the frequency domain using an iterative contracting volume integral equation approach (Pankratov et al., 1995; Singer and Fainberg, 1995). The solver has been shown to simulate electromagnetic fields of models with sharp contrasts and complicated geometries in an efficient and accurate manner (Kelbert et al., 2014; Sachl et al., 2019). The solver is forced with the computed monthly ocean tide-induced electric currents and conductance distributions (Velímský et al., 2018).

The resulting ocean tide-induced electromagnetic fields (B_{M2}) are computed at sea level and satellite altitude with a spatial resolution of 0.5° supporting information. The B_{M2} fields can be expanded into poloidal and toroidal magnetic modes with the Helmholtz decomposition (Chave and Luther, 1990). While toroidal magnetic fields are confined inside the ocean and the sediments, poloidal magnetic fields are measurable outside of the ocean as the radial magnetic field amplitudes $B_{M2,r}$ (Dostal et al., 2012). Recent studies have shown that lateral conductivity variations allow an exchange of energy between the magnetic modes (Velímský et al., 2019). In this study, however, we focus solely on $B_{M2,r}$ and do not show the remaining electromagnetic field components.

3. Results

3.1. Mean Seasonal Variations of Averaged Radial Ocean Tide-Induced Magnetic Field Amplitudes

Amplitudes of the radial ocean tide-induced magnetic field components $B_{M2,r}$ were averaged over the entire time span covered by the CORA data set. The resulting global distribution of averaged M2-induced magnetic field amplitudes is shown in Figure 1. The distributions at sea level and satellite altitude are consistent with the findings of previous studies (Grayver et al., 2016; Kuvshinov, 2008; Sabaka et al., 2016; Saynisch et al., 2016, 2017; Tyler et al., 2003).

There are four large areas with amplitudes greater than 3.0 nT at sea level and 1.4nT at satellite altitude. The strongest maximum is located around New Zealand with values of up to 6.9nT (1.7nT at satellite altitude). In the northern Atlantic $B_{M2,r}$ amplitudes reach values of 5.7nT (2.1nT), while in the Indian Ocean and the northern Pacific values of 3.0nT (1.9nT) and 3.3nT (1.4nT) are reached.

Additionally, there are multiple small-scale regions with high amplitudes at sea level but moderate amplitudes at satellite altitude. Around Madagascar, for example, $B_{M2,r}$ amplitudes reach values of 4.1nT and in the Bering Sea, close to the Aleutian Islands, they reach values of 5.7 nT. Furthermore, $B_{M2,r}$ amplitudes

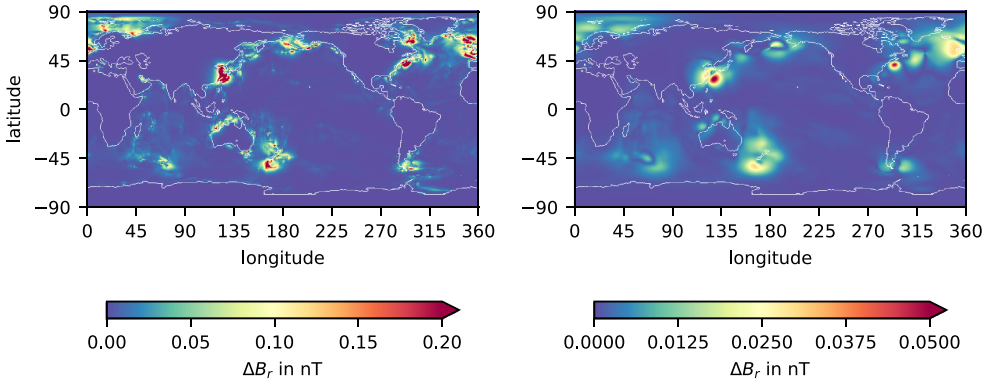

Figure 2. Seasonal peak-to-peak difference of radial ocean tide-induced magnetic fields based on climatology derived from CORA5.0 at sea level (left) and satellite altitude (right).

close to the Hudson Straight estuary in the Labrador Sea reach maximum values of 4.2 nT. These values are comparable to those occurring off the coast of Nova Scotia with maximum values of 3.7 nT. With increasing altitude, the magnitude of $B_{M2,r}$ amplitudes decreases and the lateral fine-scale structures fade until the large-scale patterns dominate and overshadow small-scale patterns. The small-scale patterns are therefore better detectable at sea level (cf. Figure 1).

In the next step, we calculated a climatological mean annual cycle from the $B_{M2,r}$ time series. The local peak-to-peak difference of the cycle represents the statistical annual modulation of $B_{M2,r}$ amplitudes and is shown in Figure 2. Areas with large peak-to-peak difference are most affected by the seasonal cycle. The computed spatial distribution of seasonal amplitude variations at satellite altitude is consistent with the one of Grayver et al. (2016).

At sea level, the largest seasonal peak-to-peak differences are found in the Yellow Sea ($\Delta B_{r,mean} \leq 0.54$nT) and Gulf of Maine ($\Delta B_{r,mean} \leq 0.68$nT). Since the mean signal in these regions is in the order of 1.0 nT, the seasonal variation represents relative changes of $\propto$10%. Off the coast of New Zealand, the Labrador Sea and off the European Atlantic coast, we also find high seasonal $B_{M2,r}$ variations with values of more than 0.3 nT.

The range at satellite altitude is about 10 times lower and reaches ≈0.05 nT in the Yellow Sea and the Gulf of Maine. Around New Zealand and the northern Atlantic the seasonal variations reach up to ≈0.03 nT. There are several reasons against the extraction of seasonal $B_{M2,r}$ amplitude variations at satellite altitude. The absolute magnetometers of the Swarm mission have a nominal accuracy of <0.045 nT (Jager et al., 2010). Furthermore, lunar tidal forces induce additional electromagnetic signals in the ionosphere (Matsushita, 1967) in the same frequency range, which have to be separated correctly. And last but not least, recent studies relied on more than 18 month of satellite data to extract global $B_{M2,r}$ amplitude fields (Grayver and Olsen, 2019; Sabaka et al., 2015, 2016, 2018; Tyler et al., 2003). Consequently, the accuracy and precision of the available data as well as the temporal sampling are momentarily too low for the task at hand.

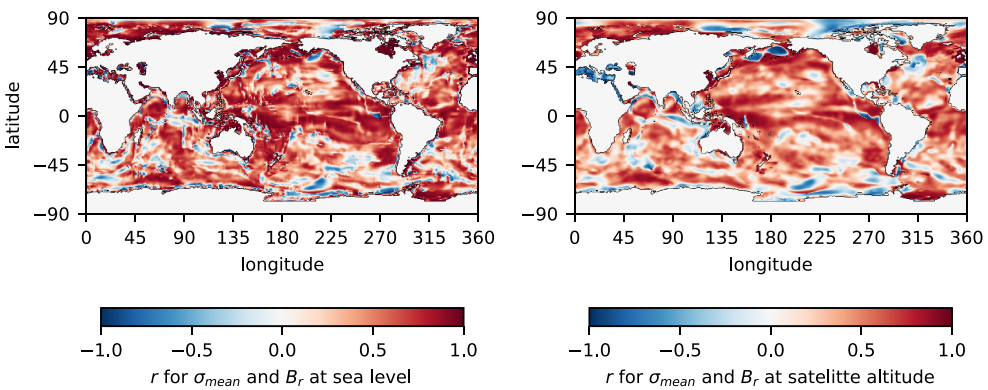

Figure 3. Pearson correlation coefficient r of σ_{mean} and B_r at sea level (left) and at satellite altitude (right).

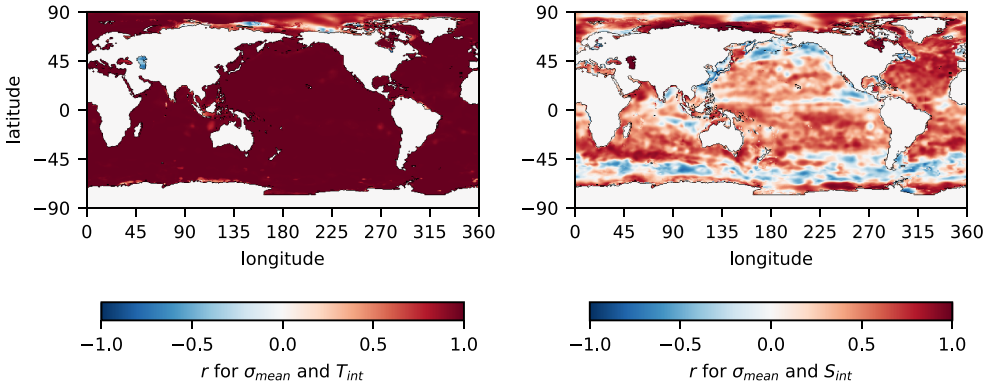

Figure 4. Pearson correlation coefficient r of σ_{mean} and T_{int} (left) and S_{int} (right).

3.2. Indications for Climate Variation

The oceanic temperature T and salinity S fields of the CORA5.0 data set are the only time-varying input in our experimental setup. The changes of S and T cause variations of the depth-averaged seawater conductivity σ_{mean}, which leads consequently to variations in the current sheet density of the ocean tide-induced electric current $\vec{j}_{M2}$ (cf. equation (1)) and the global conductance model (cf. section 2.2).

We have computed the correlation (r) between the time series of σ_{mean} and the principal lunar tide-induced radial magnetic field component $B_{M2,r}$ at sea level and satellite altitude for each grid point (cf. Figure 3). This way we are able to assess the linearity of the relation of the input and output variables. We find that r is generally close to 1 in most ocean regions. In some small regions, however, the correlation coefficient is either negative or close to 0. These exceptions are mostly found in regions with low $B_{M2,r}$. With the continuation of $B_{M2,r}$ in radial direction up to satellite altitude, the correlation decreases slightly but retains a high level.

Changes in oceanic conductivity can be attributed, in large part, to changes in the seawater temperature distribution (Saynisch et al., 2016; Tyler et al., 2017). The seawater temperature distribution is closely related to the ocean heat content, a well-known indicator for the global climate state (Meyssignac et al., 2019), which has been subject of many studies (Hansen et al., 2010; Levitus et al., 2001, 2012; Loeb et al., 2012). It is in first order proportional to the depth-integrated seawater temperature of the upper 2,000 m (Levitus et al., 2012) of the ocean; the depth for which observations are available from the Argo program (Roemmich et al., 2009). We calculated the correlation between the time series of σ_{mean} and T_{int}, the seawater temperature integrated from a depth of 2,000 m to sea surface, at each grid point (cf. figure 4) and found that T_{int} and σ_{mean} are virtually proportional in the majority of ocean regions. The correlation of both quantities is practically 1 throughout the world ocean except for regions at the immediate coast and the Arctic Ocean. In some parts of the cold Arctic Ocean we find that the changes in σ_{mean} correspond better to the depth-integrated seawater salinity S_{int} (cf. right side of Figure 4). This is explained with the fact that temperatures in that region are quite constant while the salinity exhibits much higher variability than most ocean regions. This is due to effects caused by ice formation and melting processes as well as the supply of freshwater due to glacial melting. This is in agreement with the findings of Trossman and Tyler (2019) who previously have investigated the high correlation between OHC and σ_{mean}.

Following the presented evidence, we conclude that our findings for OHC or the comparable T_{int} are also true for σ_{mean}. Additionally, we conclude that the relation of OHC and $B_{M2,r}$ is also in first order linear in most ocean regions. This makes not only the OHC and σ_{mean} but also $B_{M2,r}$ a good indicator for the oceanic climate state.

In order to assess developments in the ocean climate and compare these to the presented Greenland glacial melting (Saynisch et al., 2016) and oceanic warming (Saynisch et al., 2017) scenarios, we computed long-term trends of the depth-integrated temperature T_{int}, σ_{mean} and $B_{M2,r}$. In detail, we have carried out a linear regression to fit the linear model

$$f_i = a_1 \cdot t_i + a_0. \tag{2}$$

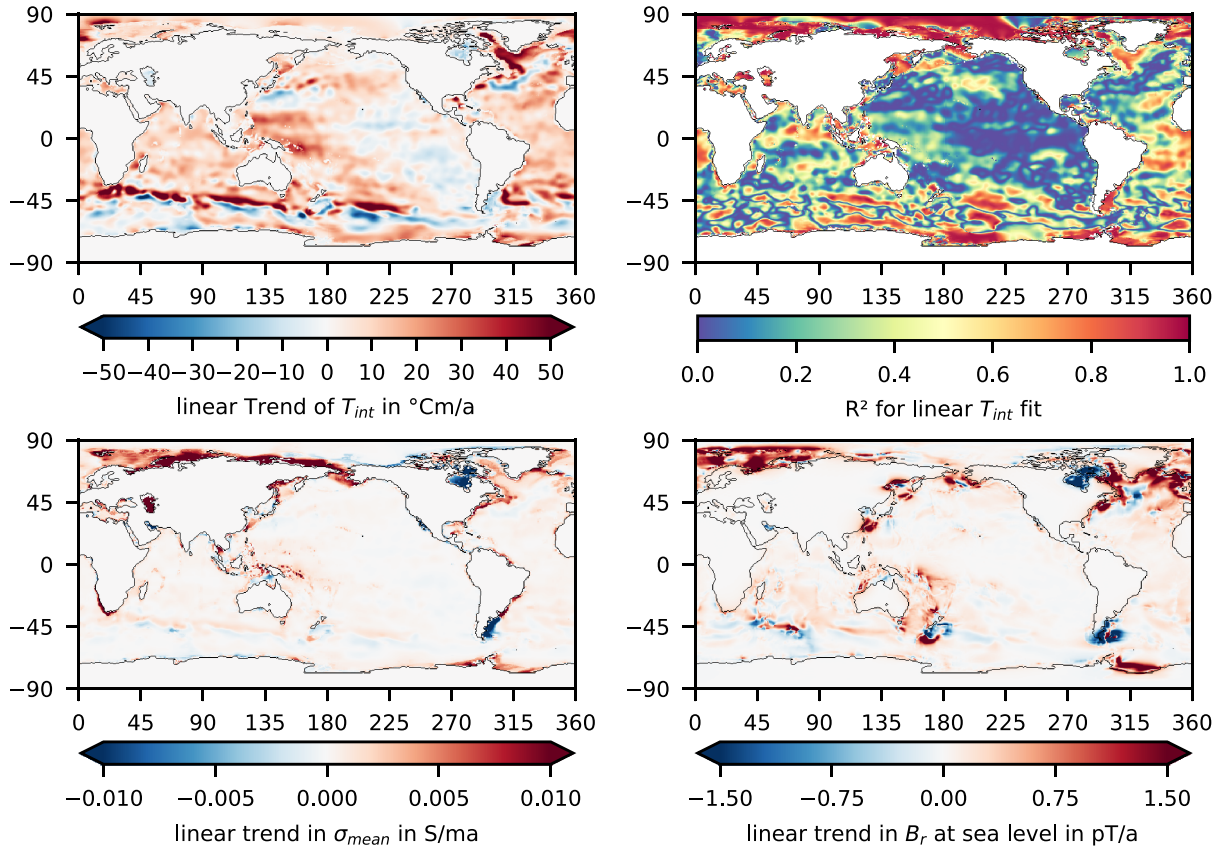

Figure 5. Linear trend in T_{int} (top left) and the corresponding coefficient of determination R^2 (top right). The linear trends in σ_{mean} (bottom left) and $B_{M2,r}$ at sea level (bottom right) follow the trend in the depth-integrated temperature T_{int} but express larger differences in their magnitude between coastal regions and the open ocean.

Here, f_i is the modeled value at time t_i. This way, we have obtained the linear trend a_1 for the entire time series (cf. Figure 5).

We have also carried out a polynomial regression of second order to fit a quadratic model

$$f_i = b_2 \cdot t_i^2 + b_1 \cdot t_i + b_0 \tag{3}$$

and obtain the quadratic trend b_2 of the time series (cf. Figure 6); a_1 and b_2 are the coefficients of the terms that will dominate the dynamic of their model in time, due to the leading exponent. In our study, b_2 is about 10 times smaller than a_1. Consequently, if the quadratic trends persist, they will dominate ocean dynamics on decadal time scales.

The coefficient of determination R^2 provides a measure of how well the observed values are explained by a model and is defined as follows:

$$R^2 := 1 - \frac{\sum_i (y_i - f_i)}{\sum_i (y_i - \bar{y})}. \tag{4}$$

Here, $\bar{y}$ is the mean of the observed values y_i and f_i is the value modeled with the respective regression fit. In order to increase the significance of R^2, we removed seasonal and high-frequency variations by applying a 12-month running mean. As a consequence, the magnitude of R^2 is increased and the decision of whether the linear or the quadratic model fits the long-term ocean dynamics better is facilitated. Due to the high correlation of $B_{M2,r}$, σ_{mean} and T_{int}, this report only illustrates the R^2 coefficient for the T_{int} model (cf. Figures 5 and 6). The R^2 coefficients of the models for $B_{M2,r}$ amplitude and σ_{mean} dynamics exhibit a very similar global distribution (not shown).

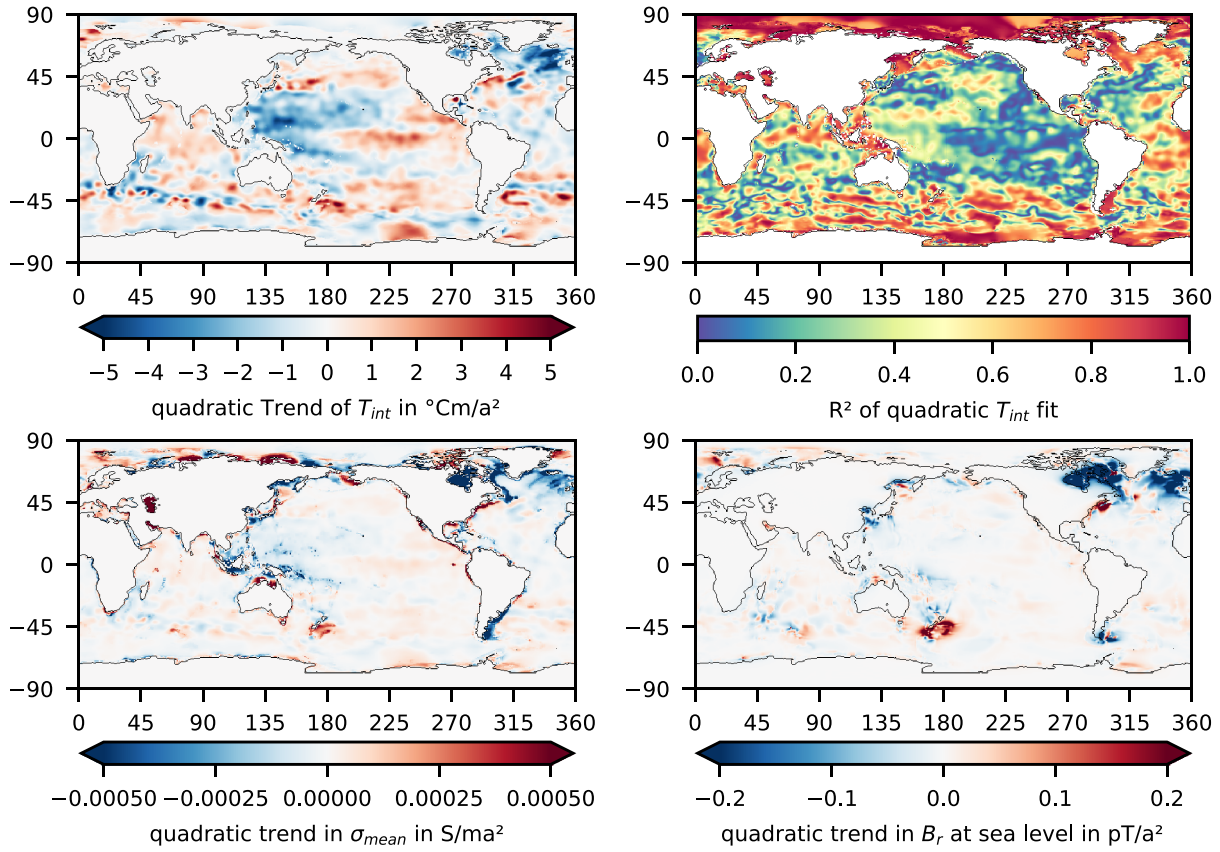

Figure 6. Quadratic trend in T_{int} (top left) and the corresponding coefficient of determination R^2 (top right) along with the quadratic trends in σ_{mean} (bottom left) and $B_{M2,r}$ at sea level (bottom right).

The distribution of signs in T_{int}, σ_{mean} and $B_{M2,r}$ trends are in good agreement. This is in accordance to the high correlation of these quantities in most ocean regions (cf. Figures 3 and 4). Despite this high correlation, there is a significant difference in the magnitude distribution in the respective trends. The magnitude of T_{int} trends is almost uniformly distributed across the global ocean. By contrast, σ_{mean} and $B_{M2,r}$ trends are about 10 times larger in the shallow shelf regions than the open ocean. This is also found for the magnitude distributions of seasonal variations in $B_{M2,r}$ (cf. Figure 2).

The complex dynamical system of the global ocean circulation, and thus of the ocean heat distribution, exhibits high variability. The dynamics are too complex to be modeled with simple linear or quadratic dynamical models on longer time scales. The dynamics of the equatorial Pacific Ocean, for example, is largely dominated by the influence of the El Niño/Southern Oscillation. In this region, R^2 values of both trend models are especially low. Neither the linear model nor the quadratic model can adequately represent the dynamic in this region. However, there are ocean regions, where ocean heat dynamics are well explained with one of these simple models.

The Arctic Ocean, the Sea of Okhotsk, the area around the Aleutian Islands, the western coast of South America, and the Weddell Sea are examples for regions for which the linear model is a good fit. That is why we find large R^2 coefficients for this model in these regions (cf. Figure 5. Additionally, the linear $B_{M2,r}$ trends in these ocean regions are relatively large, surpassing 2pT/a at sea level (0.5pT/a at satellite altitude). The trends in these regions are all positive, except for trends off the western coast of South America. Here, the OHC increases gradually in time. This agrees well with known OHC trends (Cheng et al., 2016; Levitus et al., 2012). However, the large part of ocean dynamics is poorly explained with a linear model.

The signs of b_2 and a_1, the leading exponents in the individual models, are opposed in most ocean regions. This indicates trend reversals, an acceleration or deceleration of the observed trend, or a saturation effect. In most regions, we also find a substantial increase of the R^2 coefficients for the quadratic model (cf. Figure 6).

This increase indicates that the dynamics in these regions are better fitted with the quadratic model. But only in regions where R^2 is close to 1 for the quadratic model, we can assume that T_{int}, σ_{mean} and $B_{M2,r}$ dynamics are well explained by the model.

In the northern Atlantic, south of Greenland, we find an initial increase in T_{int}, σ_{mean} and $B_{M2,r}$ over the first 15–20 years of the investigated period. However, after the tipping point between 2005 and 2010 we find a rapid decrease in both quantities. This is well represented in the fitted models. For the linear models, we find large positive trends in T_{int}, σ_{mean}, and $B_{M2,r}$, which account for the long period of increase. However, due to a reversal of the trend we find low R^2 coefficients for the linear fit. The trend reversal and the subsequent rapid decrease explain the large negative values for the quadratic T_{int}, σ_{mean}, and $B_{M2,r}$ trends and the increase in R^2 coefficients. This is also in agreement with the positive linear trends b_1 (not shown). Consequently, the linear trend of the quadratic fit dominates on shorter time scales while on longer time scales the negative quadratic trend prevails. A similar dynamic, with reversed signs, can be on the continental shelf of New Zealand.

4. Discussion

In the following we discuss effects that were neglected in our analysis but have to be taken into account when investigating actual magnetometer observations.

OHC changes in an ocean depth below 2,000 m were not taken into account in this study. However, the majority of the total OHC is stored above 700 m and the small fraction of OHC originating from depths below 2,000 m increases comparatively slow (Cheng et al., 2016). In addition, the variability of oceanic temperatures and salinity is higher in the upper ocean than in the deep ocean. Consequently, no significant changes are expected when including deep ocean salinity and temperature variations of the considered time period.

The large-scale temporal variability of the geomagnetic field and the tidal ocean flow have also been neglected. It is known that the amphidromic system is robust with regards to changes in sea level and oceanic temperatures (Saynisch et al., 2016) in the majority of ocean regions. Consequently, in those regions long-term changes in tidal amplitudes can be neglected. However in coastal regions, oceanic warming and sea level rise has a considerable impact on M2 tidal amplitudes. Seasonal warming, for example, increases coastal M2 tidal amplitudes up to 5% (Müller et al., 2014). The subsequent increase in the tidal flow, determined by the tidal amplitude and ocean depth, should in principle cause even larger seasonal $B_{M2,r}$ variations than those found in section 3.1.

4.1. Comparison to Climate Projections

There are two studies investigating the relation between oceanic climate variations and $B_{M2,r}$ anomalies. In the first study, Saynisch et al. (2017) analyzed the effects of oceanic warming, due to increased greenhouse gas content in the atmosphere, on $B_{M2,r}$ amplitudes. An initial mean annual ocean state was modeled and compared to terminal mean annual ocean states that were projected 96 years into the future. The terminal mean annual ocean states were modeled with an ocean general circulation model. The ocean model was forced with atmospheric data of a selection of atmospheric warming scenarios from CMIP5 (Taylor et al., 2012). The resulting oceanic warming caused $B_{M2,r}$ anomalies of up to 0.3 nT at sea level. The areas with largest $B_{M2,r}$ amplitude increase were the northern Atlantic, the Arctic Ocean, the Pacific region surrounding New Zealand, the Labrador Sea, the Gulf of Maine, and the northwestern Pacific. In the Hudson Bay, by contrast, $B_{M2,r}$ amplitudes decreased by a comparable magnitude.

In Saynisch et al. (2016), the second study, the authors investigated the effect of Greenland glacial melting on the ocean tide-induced magnetic field. Ongoing Greenland glacial melting was modeled with an increased freshwater influx in the northern Atlantic. The fresh water hosing experiment resulted in a breakdown of AMOC and large-scale changes in the oceanic temperature and salinity distribution. The AMOC breakdown occurred within a time period of 50–100 years. Again, the final and terminal mean annual ocean climate state were compared and revealed mostly negative $B_{M2,r}$ anomalies. At sea level, the fresh water hosing caused a decrease in $B_{M2,r}$ amplitudes in large areas around New Zealand and in the northern Atlantic. In those regions anomalies were in the order of 0.1 nT with a maximum value of 0.7 nT.

The distribution of positive and negative linear $B_{M2,r}$ matches the expectations of the oceanic warming-induced $B_{M2,r}$ anomalies modeled by Saynisch et al. (2017). The linear trends (cf. section 3.2) reach

amplitudes of more than 2pT/a in the regions where the largest $B_{M2,r}$ anomalies are expected, according to the oceanic warming scenario. Consequently, extrapolating the linear trends 100 years into the future results in $B_{M2,r}$ anomalies of more than 0.2 nT. Therefore, the changes of OHC are within the expected range. Despite the high correspondence of the linear trends and the modeled $B_{M2,r}$ anomalies of the oceanic warming study, the dynamics in the region of the northern Atlantic are better explained with a linear model.

In this study, the observed dynamics of $B_{M2,r}$ amplitudes in the northern Atlantic are well explained with the quadratic model (cf. section 3.2). The long-term trends indicated by the negative b_2 match the findings of the Greenland glacial melting study. The b_2 coefficients for the quadratic $B_{M2,r}$ model at sea level reach values of more than $0.2\text{pT}/a^2$. For the quadratic model, with b_2 coefficients about 10 times smaller than b_1 coefficients, the leading exponent will dominate the dynamic on decadal time scales. Assuming that the prospective course of the dynamics in the Northern Atlantic follows the fitted dynamic, it would take about 28 years to cause anomalies of 0.1 nT and about 55 years to cause anomalies of 0.5 nT. Neglecting the 10 times larger positive b_1 trends, this time would be reduced to about 22.5 years and 50 years, respectively. Consequently, the quadratic trends of the quadratic model also match the expected changes in OHC.

In the northern Atlantic ocean region, ocean dynamics are highly variable and cause high variability in oceanic temperature and salinity (McCarthy et al., 2015). It is also a crucial region for the global climate, because of the poleward heat transport in the Atlantic, which is unique among global oceans (Bryden and Imawaki, 2001). In the Northern Hemisphere, up to one quarter of global poleward atmosphere-ocean heat transport is carried by the AMOC. On one hand, the better fitting negative quadratic model and the decrease of AMOC during 2009–2010 for a time period of 14 months (Bryden et al., 2014) are arguments for the Greenland glacial melting scenario. On the other hand, the consistent increase in global OHC and global mean surface temperatures are in favor of the oceanic warming scenario.

The trends of both fitted models indicate developments in the ocean climate state that could lead to anomalies similar to the two presented climate scenarios. However, in the preceding studies only anomalies of the initial and the final ocean climate states have been investigated. The ocean dynamics leading to these anomalies have been neglected. By contrast, the present study investigates the dynamical changes of present day OHC and $B_{M2,r}$ amplitude variations. In consideration of the high variability of the complex ocean dynamics, especially in the North Atlantic, the investigated time period is too short to make reliable predictions for prospective ocean dynamics. The $B_{M2,r}$ amplitude changes observed in the northern Atlantic could be caused by an impending break down of AMOC but also by a temporary weakening. Additionally, the combined effects of oceanic warming and Greenland glacial melting on $B_{M2,r}$ amplitudes is currently unknown. Consequently, a longer time series of data is necessary to decide which one of the possible scenarios will prevail.

4.2. Climate Sensitive Shelf Regions

The extraction of $B_{M2,r}$ amplitudes from magnetometer observations is a challenging task. The ocean tide-induced magnetic signals are minute compared to other magnetic signals. Additionally, seasonal variations and trends in $B_{M2,r}$ amplitudes are even smaller and their detection cannot be assured for the immediate future. However, if $B_{M2,r}$ amplitude variations caused by ocean heat variations are detected, they are most likely detected in shallow ocean regions. $B_{M2,r}$ amplitudes show higher sensitivity to ocean climate variations in the shelf seas compared to the rest of the ocean. The highest seasonal variability of the $B_{M2,r}$ amplitudes (cf. figure 2) and the largest magnitude of long-term $B_{M2,r}$ trends are found in coastal regions (cf. Figures 5 and 6). This is consistent with $B_{M2,r}$ anomalies modeled in the oceanic warming and the Greenland glacial melting study (Saynisch et al., 2016, 2017).

Despite the fact that ocean depth in shelf regions is 1 order of magnitude lower than in the open ocean, there is no significant difference in the magnitudes of $B_{M2,r}$ amplitudes and the tidal ocean transports between those two regions. For the tidal transports in shelf regions, the shallow ocean depth is compensated by high tidal current velocities. As a shallow water wave, the phase velocity of the tidal wave is proportional to the square root of the ocean depth $\sqrt{h}$. However, the tidal current velocity is proportional to the product of $\sqrt{g/h}$ and the tidal elevation amplitude A (Stride, 1983). A itself is proportional to $\sqrt[-4]{h}$. Consequently, as the tidal wave approaches the shelf, tidal wave speed decreases but amplitude and current velocity increase, due to energy conservation. This explains why ocean depth has only little influence on $B_{M2,r}$ and V amplitudes but does not explain the differences in $B_{M2,r}$ sensitivity of the two ocean regimes.

The only time-variable input in our experiment design is the oceanic temperature and salinity fields. They are the only possible cause for trends and anomalies in $B_{M2,r}$ (cf. equation (1)). The tidal transports V_{M2} show only small dependence on variations of ocean depth, salinity, and temperature. The geomagnetic field B_{Earth} is independent of those quantities. This means that the increased $B_{M2,r}$ variability in shelf regions must be caused by σ_{mean} variations due to changes in the oceanic temperature and salinity distribution.

The σ_{mean} values are more extreme in shelf regions compared to the open ocean. For shelves in the midlatitude, σ_{mean} is much higher than in the deep ocean. This relation reverses in high latitudes (cf. Saynisch et al. 2016; Trossman and Tyler 2019; Tyler et al. 2017). However, the extreme values do not explain the increased sensitivity of σ_{mean} and $B_{M2,r}$ toward changes in T_{int}. Neither large temperature nor salinity changes are limited to shelf regions. In the equatorial Pacific, for example, the El Niño/Southern Oscillation causes large temperature and salinity anomalies which again cause only minor σ_{mean} and $B_{M2,r}$ anomalies (Petereit et al., 2018).

Temporal trends of T_{int} and therefore OHC are in the same order of magnitude throughout the world ocean. By contrast, the temporal trends of the highly correlated σ_{mean} are 10 times larger in shallow ocean regions (cf. Figures 5 and 6). This is explained with the fact, that the amount of heat, necessary to increase the average conductivity in the water column in shelf region, is about 10 times smaller than the amount of heat needed to cause a similar change in the open ocean. Consequently, the depth-averaged seawater conductivity σ_{mean} is more sensitive to temperature and salinity changes in shallow ocean regions than in the open ocean. That is why, the impact of oceanic temperature related phenomena like seasonal thermocline depth variations or oceanic warming on σ_{mean} and consequently $B_{M2,r}$ is 10 times larger in shelf regions than in the open ocean.

5. Summary and Conclusions

In previous ocean tide-induced magnetic field signal studies, it was investigated how the processes of Greenland glacial melting (Saynisch et al., 2016) and oceanic warming (Saynisch et al., 2017) affect climate sensitive ocean tide-induced magnetic field ($B_{M2,r}$) amplitudes in time. The findings of these studies showed opposing effects on $B_{M2,r}$ amplitudes. Therefore, in this paper we investigated how present day developments in ocean climate influence $B_{M2,r}$ amplitudes and how the present day $B_{M2,r}$ amplitude developments compare to the modeled climate scenarios. From global monthly mean seawater temperature and salinity fields, we derived a time series of global monthly mean $B_{M2,r}$ amplitudes for the years of 1990 to 2016. From the obtained $B_{M2,r}$ time series, we inferred the seasonal variability and fitted linear and quadratic trend models. This way, we assessed long-term trends in $B_{M2,r}$ amplitudes.

The linear $B_{M2,r}$ trends correspond well with the $B_{M2,r}$ anomalies caused by oceanic warming. However, these trends are in conflict with the in situ observations in the North Atlantic Ocean region. Here, $B_{M2,r}$ signals increase until a tipping point is reached toward the end of the first decade of the new millennium. Afterward, $B_{M2,r}$ amplitudes decrease continuously. This temporal development fits better to the dynamic of a quadratic model. The quadratic fit supports the findings of the Greenland glacial melting study.

Additionally, we show that ocean heat content (OHC) and $B_{M2,r}$ are highly correlated. Consequently, the found long-term $B_{M2,r}$ trends show that recent developments in OHC are within the expected range set by the two climate scenarios. In order to come to a final decision in this matter, a continuous monitoring of either OHC or ocean conductance variations is necessary. Due to the high correlation, the radial ocean tide-induced magnetic field amplitudes are a suitable observation technique for this task.

The presented variations in $B_{M2,r}$ amplitudes caused by changes in OHC are very small. It is already challenging to extract $B_{M2,r}$ amplitudes from magnetic field observations. There are further electromagnetic phenomena such as solar quiet variation or lunar tides in the ionosphere in the same frequency range. Additionally, the magnitude of the presented variations is, in most ocean regions, below the current accuracy of most magnetometer measurements. We show that their detection will most likely be realized in shallow ocean regions. Changes in electrical seawater conductivity caused by variations in oceanic temperature and salinity distribution lead to 10 times larger $B_{M2,r}$ amplitude variations in shelf regions than in the deep ocean. In the shelf regions, depth-averaged electrical seawater conductivity σ_{mean} and $B_{M2,r}$ amplitudes show high sensitivity to seasonal variations and long-term climate trends. This is explained by the fact that ocean heat variations leading to σ_{mean} changes scale with the depth of the water column. Thus, the effect of seasonal thermocline depth variations on σ_{mean}, for example, is 10 times larger in shelf seas than in the 10 times

deeper open ocean. The corresponding $B_{M2,r}$ amplitude anomalies in the shelf regions are also approximately 1 order of magnitude higher than in the deep ocean.

The seasonal $B_{M2,r}$ variability has to be taken into account when $B_{M2,r}$ amplitudes are to be extracted from magnetometer observations. A temporal averaging over a time span other than a multiple of the seasonal cycle would impose a bias. However, the current satellite magnetometer precision is too low and extracted $B_{M2,r}$ amplitudes might be unaffected by the mentioned bias.

However, there are several additional observation techniques that allow a monitoring of ocean tide-induced electromagnetic field components, like terrestrial magnetometer stations. Coastal seafloor voltage cables (Baringer and Larsen, 2001; Kuvshinov et al., 2006; Thomson et al., 1986) or ocean-bottom magnetometer (Guzavina et al., 2018; Schnepf et al., 2014, 2015; Shimizu et al., 2011) even allow detection of components other than $B_{M2,r}$.

We conclude that oceanic shelves are not only the regions where $B_{M2,r}$ amplitudes are most affected by oceanic climate variations but also the regions where these climate variations will become observable as $B_{M2,r}$ variations first. Consequently, a targeted monitoring of ocean tide-induced magnetic fields in shelf regions is beneficial for the monitoring of changes in oceanic and therefore Earth's climate. As a next step, it is planned to extract seasonal and long-term $B_{M2,r}$ amplitude variations from coastal magnetometer observations to test the presented results.

Acknowledgments
The work described in this paper has received funding from the German Research Foundation's priority program 1788 "Dynamic Earth" and the Initiative and Networking Fund of the Helmholtz Association through the project "Advanced Earth System Modelling Capacity (ESM)." We acknowledge the generation and distribution of the TPXO tidal data. We also want to thank Alexey Kuvshinov for kindly providing his 3-D EM induction code and the model of mantle conductivity. The published data set Petereit et al. (2019) provides the complete time series data of the computed global ocean tide-induced electromagnetic field signals. The data are permanently available at the public research data repository GFZ Data Services (DOI: http://doi.org/10.5880/GFZ.1.3.2019.001).

References

Baringer, M. O., & Larsen, J. C. (2001). Sixteen years of Florida current transport at 27° N. *Geophysical Research Letters*, *28*, 3179–3182. https://doi.org/10.1029/2001GL013246

Bretherton, F. P., Davis, R. E., & Fandry, C. (1976). A technique for objective analysis and design of oceanographic experiments applied to MODE-73. *Deep Sea Research and Oceanographic Abstracts*, 23(7), 559–582. https://doi.org/10.1016/0011-7471(76)90001-2

Bryden, H. L., & Imawaki, S. (2001). Chapter 6.1 Ocean heat transport. In G. Siedler, J. Church, & J. Gould (Eds.), *Ocean Circulation and Climate*, International Geophysics (Vol. 77, pp. 455–474). Academic Press. https://doi.org/10.1016/S0074-6142(01)80134-0

Bryden, H. L., King, B. A., McCarthy, G. D., & McDonagh, E. L. (2014). Impact of a 30% reduction in Atlantic meridional overturning during 2009 – 2010. *Ocean Science*, *10*(4), 683–691. https://doi.org/10.5194/os-10-683-2014

Cabanes, C., Grouazel, A., von Schuckmann, K., Hamon, M., Turpin, V., Coatanoan, C., et al. (2013). The CORA dataset: Validation and diagnostics of in-situ ocean temperature and salinity measurements. *Ocean Science*, *9*(1), 1–18. https://doi.org/10.5194/os-9-1-2013

Chave, A. D., & Luther, D. S. (1990). Low-frequency, motionally induced electromagnetic fields in the ocean: 1 Theory. *Journal of Geophysical Research*, *95*(C5), 7185–7200.

Cheng, L., Trenberth, K. E., Palmer, M. D., Zhu, J., & Abraham, J. P. (2016). Observed and simulated full-depth ocean heat-content changes for 1970–2005. *Ocean Science*, *12*(4), 925–935. https://doi.org/10.5194/os-12-925-2016

Dostal, J., Martinec, Z., & Thomas, M. (2012). The modelling of the toroidal magnetic field induced by tidal ocean circulation. *Geophysical Journal International*, *189*(2), 782–798. https://doi.org/10.1111/j.1365-246X.2012.05407.x

Egbert, G. D., & Erofeeva, S. Y. (2002). Efficient inverse modeling of barotropic ocean tides. *Journal of Atmospheric and Oceanic Technology*, *19*(2), 183–204.

Everett, M. E., Constable, S., & Constable, C. G. (2003). Effects of near-surface conductance on global satellite induction responses. *Geophysical Journal International*, *153*(1), 277–286.

Gaillard, F., Reynaud, T., Thierry, V., Kolodziejczyk, N., & von Schuckmann, K. (2016). In situ-based reanalysis of the global ocean temperature and salinity with ISAS: Variability of the heat content and steric height. *Journal of Climate*, *29*(4), 1305–1323. https://doi.org/10.1175/JCLI-D-15-0028.1

Gillet, N., Lesur, V., & Olsen, N. (2010). Geomagnetic core field secular variation models. *Space Science Reviews*, *155*(1), 129–145.

Grayver, A. V., Munch, F. D., Kuvshinov, A. V., Khan, A., Sabaka, T. J., & Tøffner-Clausen, L. (2017). Joint inversion of satellite-detected tidal and magnetospheric signals constrains electrical conductivity and water content of the upper mantle and transition zone. *Geophysical Research Letters*, *44*, 6074–6081. https://doi.org/10.1002/2017GL073446

Grayver, A. V., & Olsen, N. (2019). The magnetic signatures of the M2, N2, and O1 oceanic tides observed in swarm and champ satellite magnetic data. *Geophysical Research Letters*, *46*, 4230–4238. https://doi.org/10.1029/2019GL082400

Grayver, A. V., Schnepf, N. R., Kuvshinov, A. V., Sabaka, T. J., Manoj, C., & Olsen, N. (2016). Satellite tidal magnetic signals constrain oceanic lithosphere-asthenosphere boundary. *Science Advances*, *2*(9). https://doi.org/10.1126/sciadv.1600798

Guzavina, M., Grayver, A., & Kuvshinov, A. (2018). Do ocean tidal signals influence recovery of solar quiet variations? *Earth, Planets and Space*, *70*(1), 5. https://doi.org/10.1186/s40623-017-0769-1

Hansen, J., Ruedy, R., Sato, M., & Lo, K. (2010). Global surface temperature change. *Reviews of Geophysics*, *48*, RG4004. https://doi.org/10.1029/2010RG000345

Hayes, S., Mangum, L., Picaut, J., Sumi, A., & Takeuchi, K. (1991). TOGA-TAO: A moored array for real-time measurements in the tropical Pacific Ocean. *Bulletin of the American Meteorological Society*, *72*(3), 339–347.

IOC, SCOR, & APSO (2010). The International thermodynamic equation of seawater–2010: Calculation and use of thermodynamic properties, Intergovernmental Oceanographic Commission. *Manual and Guides*, *56*, 196.

Irrgang, C., Saynisch, J., & Thomas, M. (2016). Impact of variable seawater conductivity on motional induction simulated with an ocean general circulation model. *Ocean Science*, *12*(1), 129–136. https://doi.org/10.5194/os-12-129-2016

Irrgang, C., Saynisch, J., & Thomas, M. (2019). Estimating global ocean heat content from tidal magnetic satellite observations. *Scientific Reports*, *9*(7893), 2045–2322. https://doi.org/10.1038/s41598-019-44397-8

Jager, T., Léger, J.-M., Bertrand, F., Fratter, I., & Lalaurie, J. (2010). SWARM Absolute Scalar Magnetometer accuracy: Analyses and measurement results. In *SENSORS, 2010 IEEE* (pp. 2392–2395). IEEE. https://doi.org/10.1109/ICSENS.2010.5690960

Kelbert, A., Kuvshinov, A., Velímský, J., Koyama, T., Ribaudo, J., Sun, J., et al. (2014). Global 3-D electromagnetic forward modelling: a benchmark study. *Geophysical Journal International*, *197*(2), 785–814. https://doi.org/10.1093/gji/ggu028

Kuvshinov, A. (2008). 3-D global induction in the oceans and solid earth: Recent progress in modeling magnetic and electric fields from sources of magnetospheric, ionospheric and oceanic origin. *Surveys in Geophysics*, *29*(2), 139–186.

Kuvshinov, A., Junge, A., & Utada, H. (2006). 3-D modelling the electric field due to ocean tidal flow and comparison with observations. *Geophysical Research Letters*, *33*, L06314. https://doi.org/10.1029/2005GL025043

Laske, G., and G. Masters (1997), A global digital map of sediment thickness, In *EOS Transactions AGU*, vol. *78*(46), F483, Fall Meeting Supplement, Abstract S4E1-01.

Levitus, S., Antonov, J. I., Boyer, T. P., Baranova, O. K., Garcia, H. E., Locarnini, R. A., et al. (2012). World ocean heat content and thermosteric sea level change (0--2000 m), 1955-2010. *Geophysical Research Letters*, *39*, L10603. https://doi.org/10.1029/2012GL051106

Levitus, S., Antonov, J. I., Wang, J., Delworth, T. L., Dixon, K. W., & Broccoli, A. J. (2001). Anthropogenic warming of earth's climate system. *Science*, *292*(5515), 267–270. https://doi.org/10.1126/science.1058154

Locarnini, R. A., A. V. Mishonov, J. I. Antonov, T. P. Boyer, H. E. Garcia, O. K. Baranova, et al. (2013), World ocean atlas 2013. Volume 1, Temperature, *NOAA Atlas NESDIS*.

Loeb, J. M., Lyman, N. G., Johnson, G. C., Allan, R. P., Doelling, D. R., Wong, T., et al. (2012). Observed changes in top-of-the-atmosphere radiation and upper-ocean heating consistent within uncertainty. *Nature Geoscience*, *5*, 110–113. https://doi.org/10.1038/ngeo1375

Manoj, C., Kuvshinov, A., Maus, S., & Lühr, H. (2006). Ocean circulation generated magnetic signals. *Earth, Planets and Space*, *58*(4), 429–437.

Matsushita, S. (1967). Lunar tides in the ionosphere. In J. Bartel (Ed.), *Geophysik III/ Geophysics III: Teil II/Part II* (pp. 547–602). Berlin, Heidelberg: Springer. https://doi.org/10.1007/978-3-642-46082-1_2

McCarthy, G. D., Haigh, I. D., Hirschi, J. J.-M., Grist, J. P., & Smeed, D. A. (2015). Ocean impact on decadal Atlantic climate variability revealed by sea-level observations. *Nature*, *521*, 508–510. https://doi.org/10.1038/nature14491

Meyssignac, B., Boyer, T., Zhao, Z., Hakuba, M. Z., Landerer, F. W., Stammer, D., et al. (2019). Measuring global ocean heat content to estimate the Earth energy imbalance. *Frontiers in Marine Science*, *6*, 432. https://doi.org/10.3389/fmars.2019.00432

Minami, T. (2017). Motional induction by tsunamis and ocean tides: 10 years of progress. *Surveys in Geophysics*, *38*(5), 1097–1132.

Müller, M., Cherniawsky, J. Y., Foreman, M. G. G., & von Storch, J.-S. (2014). Seasonal variation of the M2 tide. *Ocean Dynamics*, *64*(2), 159–177. https://doi.org/10.1007/s10236-013-0679-0

Pankratov, O. V., Avdeyev, D. B., & Kuvshinov, A. V. (1995). Electromagnetic field scattering in a heterogeneous Earth: A solution to the forward problem. *Solid Earth*, *31*, 201–209.

Petereit, J., Saynisch, J., Irrgang, C., Weber, T., & Thomas, M. (2018). Electromagnetic characteristics of ENSO. *Ocean Science*, *14*(3), 515–524. https://doi.org/10.5194/os-14-515-2018

Roemmich, D., Johnson, G. C., Riser, S., Davis, R., Gilson, J., Owens, W. B., et al. (2009). The argo program: Observing the global ocean with profiling floats. *Oceanography*, *22*. https://doi.org/10.5670/oceanog.2009.36

Sabaka, T. J., Tøffner-Clausen, L., Olsen, N., & Finlay, C. C. (2018). A comprehensive model of Earth's magnetic field determined from 4 years of Swarm satellite observations. *Earth, Planets and Space*, *70*(1), 130. https://doi.org/10.1186/s40623-018-0896-3

Sabaka, T. J., Tyler, R. H., & Olsen, N. (2016). Extracting ocean-generated tidal magnetic signals from Swarm data through satellite gradiometry. *Geophysical Research Letters*, *43*, 3237–3245.

Sabaka, T. J., Tyler, R. H., Olsen, N., & Kuvshinov, A. (2015). CM5, a pre-Swarm comprehensive geomagnetic field model derived from over 12 yr of CHAMP, Ørsted, SAC-C and observatory data. *Geophysical Journal International*, *200*(3), 1596–1626. https://doi.org/10.1093/gji/ggu493

Sachl, L., Martinec, Z., Velímský, J., Irrgang, C., Petereit, J., Saynisch, J., et al. (2019). Modelling of electromagnetic signatures of global ocean circulation: Physical approximations and numerical issues. *Earth, Planets and Space*, *71*(1), 58. https://doi.org/10.1186/s40623-019-1033-7

Saynisch, J., Petereit, J., Irrgang, C., Kuvshinov, A., & Thomas, M. (2016). Impact of climate variability on the tidal oceanic magnetic signal---A model-based sensitivity study. *Journal of Geophysical Research: Oceans*, *121*, 5931–5941. https://doi.org/10.1002/2016JC012027

Saynisch, J., Petereit, J., Irrgang, C., & Thomas, M. (2017). Impact of oceanic warming on electromagnetic oceanic tidal signals: A CMIP5 climate model-based sensitivity study. *Geophysical Research Letters*, *44*, 4994–5000. https://doi.org/10.1002/2017GL073683

Schnepf, N. R., Kuvshinov, A., & Sabaka, T. (2015). Can we probe the conductivity of the lithosphere and upper mantle using satellite tidal magnetic signals? *Geophysical Research Letters*, *42*, 3233–3239. https://doi.org/10.1002/2015GL063540

Schnepf, N. R., Manoj, C., Kuvshinov, A., Toh, H., & Maus, S. (2014). Tidal signals in ocean-bottom magnetic measurements of the Northwestern Pacific: Observation versus prediction. *Geophysical Journal International*, *198*(2), 1096–1110. https://doi.org/10.1093/gji/ggu190

Shimizu, H., Yoneda, A., Baba, K., Utada, H., & Palshin, N. A. (2011). Sq effect on the electromagnetic response functions in the period range between 104 and 105 s. *Geophysical Journal International*, *186*(1), 193–206. https://doi.org/10.1111/j.1365-246X.2011.05036.x

Singer, B. S., & Fainberg, E. (1995). Generalization of the iterative dissipative method for modeling electromagnetic fields in nonuniform media with displacement currents. *Journal of Applied Geophysics*, *34*(1), 41–46.

Stride, A. H. (1983). Offshore tidal sands: Processes and deposits. *Journal of the Marine Biological Association of the United Kingdom*, *63*(3), 738–738. https://doi.org/10.1017/S0025315400071149

Taylor, K. E., Stouffer, R. J., & Meehl, G. A. (2012). An overview of CMIP5 and the experiment design. *Bulletin of the American Meteorological Society*, *93*(4), 485–498.

Thébault, E., Finlay, C. C., Beggan, C. D., Alken, P., Aubert, J., Barrois, O., et al. (2015). International geomagnetic reference field: The 12th generation. *Earth, Planets and Space*, *67*(1), 79. https://doi.org/10.1186/s40623-015-0228-9

Thomson, D. J., Lanzerotti, L. J., Medford, L. V., Maclennan, C. G., Meloni, A., & Gregori, G. P. (1986). Study of tidal periodicities using a Transatlantic telecommunications cable. *Geophysical Research Letters*, *13*(6), 525–528. https://doi.org/10.1029/GL013i006p00525

Trossman, D. S., & Tyler, R. H. (2019). Predictability of ocean heat content from electrical conductance. *Journal of Geophysical Research: Oceans*, *124*, 667–679. https://doi.org/10.1029/2018JC014740

Tyler, R. H., Boyer, T. P., Minami, T., Zweng, M. M., & Reagan, J. R. (2017). Electrical conductivity of the global ocean. *Earth, Planets and Space*, *69*(1), 156. https://doi.org/10.1186/s40623-017-0739-7

Tyler, R. H., Maus, S., & Lühr, H. (2003). Satellite observations of magnetic fields due to ocean tidal flow. *Science*, *299*(5604), 239–241.

Velímský, J., Grayver, A., Kuvshinov, A., & Šachl, L. (2018). On the modelling of *m*2 tidal magnetic signatures: Effects of physical approximations and numerical resolution. *Earth, Planets and Space*, *70*(1), 192. https://doi.org/10.1186/s40623-018-0967-5

Velímský, J., Šachl, L., & Martinec, Z. (2019). The global toroidal magnetic field generated in the Earth's oceans. *Earth and Planetary Science Letters*, *509*, 47–54. https://doi.org/10.1016/j.epsl.2018.12.026

Zweng, M. M., J. R. Reagan, J. I. Antonov, R. A. Locarnini, A. V. Mishonov, T. P. Boyer, et al. (2013), World ocean atlas 2013. volume 2, salinity, *NOAA Atlas NESDIS*.